Journal of MATERIALS RESEARCH

Invited Feature Paper
DOI:10.1557/s43578-023-01161-z

EARLY CAREER SCHOLARS IN MATERIALS SCIENCE, 2024

ANNUAL ISSUE

Nano-TiC-reinforced 18Ni300 steel manufactured by Powder Bed Fusion-Laser Beam with improved wear resistance for mould inserts

Daniel F. S. Ferreira[1,2,3,4,a], G. Miranda[4,5], Filipe J. Oliveira[4,5], José M. Oliveira[2,3,4]

[1] Welding and Quality Institute, Instituto de Soldadura e Qualidade (ISQ), Avenida Professor Dr. Cavaco Silva, 33 Taguspark, 2740-120 Porto Salvo, Portugal
[2] EMaRT, Emerging Materials and Research Technologies, Estrada do Cercal 449, 3720-511 Santiago da Riba-Ul, Portugal
[3] School of Design, Management and Production Technologies Northern Aveiro, Estrada do Cercal 449, 3720-511 Santiago da Riba-Ul, Portugal
[4] CICECO, Aveiro Institute of Materials, University of Aveiro, Campus Universitário de Santiago, 3810-193 Aveiro, Portugal
[5] Department of Materials and Ceramic Engineering, University of Aveiro, Campus Universitário de Santiago, 3810-193 Aveiro, Portugal
[a] Address all correspondence to this author. e-mail: dferreira@ua.pt

Received: 8 May 2023; accepted: 6 September 2023; published online: 28 September 2023

In injection moulding, surfaces can be exposed to harsh working conditions, especially when polymers reinforced with abrasive glass fibres are used. Low carbon martensitic steels, such as maraging steels, are an excellent choice for demanding and complex mould inserts produced by Powder Bed Fusion-Laser Beam (PBF-LB). However, their wear resistance is lower than that of tool steels such as AISI D2 or H13, whose PBF-LB printability is challenging, due to their carbon content that makes them susceptible to cracking. In this study, an alternative material with high printability by PBF-LB was developed, by reinforcing maraging steel 18Ni300 with nano-sized titanium carbide (TiC). TiC-reinforced 18Ni300 nanocomposites showed an improvement in microhardness of up to 23% (730 HV_2) after addition of 7.0 vol% TiC. Tribological tests against a polypropylene with 40 wt% glass fibres showed that the specific wear rate decreased by about an order of magnitude (to 0.32×10^{-6} mm^3/N m) compared to the unreinforced maraging steel.

Daniel F. S. Ferreira

Daniel F. S. Ferreira is a researcher in Additive Manufacturing (AM) at the Instituto de Soldadura e Qualidade (ISQ) in Portugal and is currently working with PBF-LB. He received his M.D. in Materials Engineering from the University of Aveiro in 2018 and completed his Ph.D. in Nanoscience and Nanotechnology at the same university in 2022. His PhD thesis focused on the development of new nanocomposites through PBF-LB with improved mechanical performance and wear resistance. His work took place in an industrial environment and focused on the mould industry, which gave him an industrial vision of the PBF-LB process and its practical application. Since 2020, Dr. Daniel Ferreira has been working as an invited Assistant Professor at the School of Design, Management and Production Technologies Northern Aveiro at the University of Aveiro. Dr. Daniel Ferreira has experience in the development of new materials for additive manufacturing, the characterization of metal powders and parts, and the optimization of parameters for the PBF-LB process, with a focus on microstructure design. His goal is to contribute to the global community, promote industrial AM adoption, and build international collaborations and recognition.

Introduction

Previous studies have shown that the Powder Bed Fusion-Laser Beam process of metals (PBF-LB/M) is capable of producing fully dense metal parts with equivalent or even higher mechanical properties than conventional processes such as casting or forging [1–3]. However, the high temperature gradients generated by localised heating of a very small area and rapid solidification can cause high residual stresses and deformation [4].

It is well known that PBF-LB of tool steels (e.g., AISI H13, H11, or D2), which are very attractive for moulds due to their excellent wear resistance, is challenging due to various defects that occur during the PBF-LB process, such as lack-of-fusion, solidification cracks, and residual stress cracks. These defects can occur due to inadequate heat input, powders with asymmetric shape, and local changes in chemical composition that are prone to occur, as discussed by Wu et al. [5]. In addition, the rapid cooling of the PBF-LB (10^5 to 10^6 K/s) leads to material cracking due to the induced volume changes [6].

Therefore, most PBF-LB studies focus on steels with little or no carbon in the chemical composition, such as 18Ni300, 316L, 304L, and 420 stainless steel [7–10]. These steels are suitable for PBF-LB and are characterised by good weldability, dimensional stability, and low residual stresses, but are less wear resistant than the carbon tool steels mentioned above [11–14]. The maraging steel 18Ni300 with extremely low carbon content (< 0.03 wt%) is one of the most promising materials for the PBF-LB process and has attracted much attention in mould making due to its combination of good plasticity, toughness, weldability and corrosion resistance [15]. Most studies reporting on PBF-LB focused on the processing of this ultra-low carbon steel because of its tendency to low stresses and good dimensional stability [7, 16]. After a simplified aging treatment in air at temperatures around 500 °C for 6 h, the tensile strength of 18Ni300 is similar to that of the reference steels for mould making (e.g. AISI H13). This makes the 18Ni300 steel very attractive for use in additively manufactured inserts with complicated designs instead of H13, H11 or D2 for the reasons mentioned above [17]. However, the wear resistance of 18Ni300 is relatively poor compared to these carbon tool steels.

The lower wear resistance of 18Ni300 can prove critical and lead to mould failure due to surface degradation, especially when abrasive media is injected, such as polymers reinforced with abrasive glass fibres [18]. The degradation of the mould surface affects the quality of the manufactured parts, increasing the likelihood of defective parts, which in turn leads to higher costs [19].

To improve the mechanical properties and wear behaviour of metallic materials, nanoparticle (NP) reinforcement has been reported recently, leading to metal matrix nanocomposites (MMNCs). These materials have received remarkable attention due to their unusual combination of mechanical and isotropic properties for demanding applications [20]. In MMNCs, a nanometer-sized (less than 100 nm) reinforcing phase is dispersed in a metallic matrix, which offers significant advantages in mechanical performance, wear, and damping properties compared to microscale reinforced composites (MMCs) [20].

In this paper, we propose to improve the wear resistance of 18Ni300 steel by fabricating 18Ni300 matrix nanocomposites using PBF-LB and understand their mechanical performance and wear mechanisms.

In PBF-LB, the high energy released by the laser beam in a short time leads to rapid solidification, which refines the microstructure and prevents segregation by effectively dispersing the reinforcing phase in the matrix [20–23]. Previous studies report the use of micro- and nanoscale reinforcements for metallic matrices, namely carbides (e.g., WC, TiC, SiC, B_4C), nitrides (e.g., Si_3N4, AlN, TiN), borides (e.g., TiB_2), or elemental materials (e.g., C, Si) [20, 24]. Chen et al. [25] reported that refractive TiC, WC, TiN and TiB_2 nanoparticles are suitable as reinforcement for steels due to their high stability and hardness as well as good wettability and similar coefficient of thermal expansion (CTE) compared to low carbon steels.

The homogeneous distribution of nanoparticles in the matrix is responsible for the improvement of mechanical properties, hardness and wear resistance [20]. Despite the growing interest in the development of nanocomposites, many studies in the literature report the use of microreinforcements instead of nanosized reinforcements due to the difficulty in finding suitable suppliers of nanoparticles in the market at industrial scale, which greatly affects the improvement of properties. For this reason, studies using micro-sized reinforcing phases are also considered in this this review.

NP content affects the final performance of MMNCs. In general, higher content leads to higher microhardness, as reported by several authors for 316L steel reinforced with WC, TiC and TiB_2 in concentrations not exceeding 15 wt% (corresponding to 8, 22 and 24 vol%, respectively) [26, 27]. However, high reinforcement concentrations can lead to a deterioration of the mechanical properties if the nanoparticles tend to agglomerate due to the van der Walls interaction at the nanoscale because of their large surface area compared to their volume [28]. Moreover, the behaviour in terms of flowability, absorption, and reactivity of powders prepared specifically for PBF-LB changes dramatically when high concentrations of NPs are added [29, 30].

TiC can be a promising reinforcement for steels, due to its mechanical properties and high wear resistance [20]. In addition, TiC has a lower density than steel (4.9 g/cm^3), so its addition to steel reduces weight. Bhowmik et al. [31] fabricated a 316L stainless steel reinforced by PBF-LB with micro-sized TiC and found that there are two arrangements of TiC carbides in the microstructure: TiC carbides distributed in the grain interior and those distributed at the grain boundaries. This arrangement of carbides in the structure of the material contributes to its strengthening by grain refinement and impeding the movement of dislocations, but it can also be the origin of defects, such as lack of fusion, which negatively affects the elongation to fracture of the material, as reported by Oliveira et al. [32] and Kahlert et al. [33].

AlMangour et al. [34] fabricated a H13 steel reinforced with 15 vol% TiC NPs with an average size of 50 nm by PBF-LB. They reported ~ 7% higher hardness and ~ 10% higher elastic modulus, as well as ~ 17% lower friction against a 2100 bearing steel

ball and ~ 26% lower wear rate, attributing these improvements to the combined effects of grain refinement and grain boundary strengthening. Li et al. [15] also reported that TiC microparticles improved the wear performance of 316L steel and refined the microstructure by reducing the cell size. The authors also investigated the strengthening mechanisms and reported that there were many dislocations near the TiC particles, which contributed to the improvement of mechanical properties, hardness, and wear resistance.

Gu et al. [29] simulated the thermal evolution behaviour during PBF-LB of an Al-matrix nanocomposite reinforced with TiC. They reported that the addition of TiC nanoparticles can significantly change the melting behaviour due to the high absorptivity of TiC (~ 82%) using an infrared laser with a wavelength of 1064 nm (for comparison, steel powder generally has an absorptivity between 30 and 40%). The authors reported that a reinforcement content of about 2.5 wt% is associated with lower heat absorption of the steel powder and therefore less intense Marangoni flow, while doubling the reinforcement content to 5 wt%, results in more intense Marangoni flow, which induces a circular flow due to the convection forced in the melt pool. A ring-like structure with uniformly distributed TiC particles was formed in the final MMNC material. Similar results were reported by AlMangour et al. [27] for a 316L stainless steel reinforced with micro- and nano- sized TiC (1 μm and 50 nm, respectively). Hao et al. [35] also reported this phenomenon for 316L stainless steel reinforced with hydroxyapatite microparticles.

Hu et al. [36] manufactured TiC-reinforced 18Ni300 composites by direct energy deposition (DED) and investigated the effects of TiC addition on the microstructure, microhardness and wear resistance of the composite material. The TiC particles, with an average size of 7 μm, were found to increase the microhardness of the composite material by 18% when added in concentrations up to 5%. In addition, the authors found that the wear resistance of the composite material against a Si_3N_4 ball increased 13 and 41 times before and after heat treatment, respectively.

To these authors knowledge, there are no publications on the wear behaviour of PBF-LB-manufactured TiC-reinforced 18Ni300 nanocomposites under conditions that nearly or fully simulate the wear that occurs in the moulds surface during the injection and subsequent removal steps.

In this sense, the present study, addresses the mechanical and wear behaviour TiC-reinforced 18Ni300 nanocomposites obtained by PBF-LB. After manufacturing and microstructure characterization, dry sliding wear tests were carried out against a commercial 40 wt% E-glass fibre reinforced polypropylene, a material commonly injection moulded to produce parts for the automotive industry. This was done aiming to evaluate the behaviour of the nanocomposites in contact with a material normally processed by injection moulding, admitting that this is a proxy and not a full replication of the wear that occurs in the moulds during injection moulding and part removal. The worn volume was evaluated using 3D optical profilometry to accurately quantify the low wear volumes. In addition, the morphology of the worn surfaces was evaluated using scanning electron microscopy (SEM) to discuss the wear mechanisms.

Selected materials and practical procedures

Feedstock preparation for PBF-LB process

The starting materials for the preparation of the nanocomposites were an 18Ni300 maraging steel, gas-atomized, nearly spherical powder (Renishaw Ltd., UK), with $D_{50} = 35$ μm and $D_{90} = 48$ μm, and TiC (Nanografi, Germany) nanometric black powder with a purity ≥ 99.5%. According to the technical data sheet, the average particle size is between 35 and 55 nm, the melting point is 3200 °C and the morphology of the powder is spherical.

The starting powders were weighed at ratios of 2.0, 4.5, and 7.0 vol% TiC to obtain 1.2 kg of starting material for PBF-LB. Then, the powders were subjected to high-energy ball milling in a metal vessel with a ball-to-powder ratio of 2:1 in a Pulverisette 6 (Fritsch, Germany) for 4 h at a speed of 200 rpm, in air. The duration of high-energy ball milling was limited to 4 h to obtain a reasonable approximation of the original spherical structure of the 18Ni300 powder and to obtain good flowability of the powder after milling [37].

PBF-LB processing and sample preparation

An AM 500Q PBF-LB series 3D printer (Renishaw Ltd., UK) equipped with a reduced build volume (RBV) with a maximum build volume of $78 \times 78 \times 55$ mm^3 was used to transform the prepared powders into dense nanocomposite parts. This machine has four ytterbium fibre lasers with 500 W and a laser spot of 80 μm. During the building process, argon shielding gas was injected into the building chamber in a closed loop and recirculated to avoid the formation of by-products. Based on our previous experience and the literature, a stripe strategy was chosen because it leads to better quality and lower residual stresses while allowing a high build rate (up to 150 cm^3/h depending on the chosen conditions and material) [38]. Each new layer was rotated 67° clockwise to minimise preferential hotspots (thermal gradients) and avoid distortion and residual stresses.

An initial assessment of processing parameters for the different nanocomposites was carries out by manufacturing six cuboid samples with different combinations of PBF-LB parameters with the aim of obtaining fully dense and microhardness improved specimens. In our previous studies [[39, 40]], a preliminary parameter optimization was performed for the production of dense and microhardness improved 18Ni300 steel by

PBF-LB. Based on the results of this study in terms of promising processing windows for this alloy, a simplified parameter evaluation was made for the new composite powders and 6 cuboid samples were fabricated.

The six combinations were obtained by varying the laser power from 100 to 500 W within the optimal parameter set used in our previous work [39], corresponding to energy densities between 26 and 133 J/mm^3. For the powder prepared with an addition of 4.5 vol% TiC, the maximum density (> 99.9%) and microhardness (468 HV_2) were obtained at a laser power of 250 W, a scanning speed of 1000 mm/s, a hatch distance of 75 µm and a layer thickness of 50 µm. These parameters were used to fabricate the nanocomposites. PBF-LB processing was performed under vacuum and oxygen content below 31 ppm.

The parts made from the different powders are designated by: MS (18Ni300); MS + 2.0TiC (18Ni300 + 2.0%vol TiC); MS + 4.5TiC (18Ni300 + 4.5%vol TiC); and MS + 7.0TiC (18Ni300 + 7.0%vol TiC).

Different specimens were made: for mechanical and wear tests, and for microhardness and density measurements. Horizontal cylinders were printed for the tensile specimens, which were then machined according to the final shape specified in ASTM E8. The pins for the tribological dry sliding tests were made in the form of cylinders with double spherical tips, which were then machined to a final length of 20 mm and a tip diameter of 8 mm. The specimens for the microhardness and density measurements were printed as discs with a diameter of 18 mm and a height of 10 mm. The specimens were separated from the metal substrate plate by electroerosion and subjected to heat treatment at 510 °C for six hours (the same aging heat treatment as for maraging steel 18Ni300), using the procedure of Yin et al. [41]. The counterparts for performing the tribological tests were discs produced by injection moulding in a 500-tonne Victory type injection moulding machine (ENGEL GmbH, Austria) from starting pellets of a semi-crystalline thermoplastic polypropylene with 40 wt% short glass fibre (Borealis, Austria).

Material's characterization and testing

Structural and microstructural analysis

Structural analysis was performed on sections of the printed discs using an optical microscope (OM) (Nikon, Japan) to evaluate the dimensions of the melt pools and identify the laser marks. In addition, SEM analysis (SU-70, Hitach, Japan) was performed to observe the microstructural details. Before taking micrographs, the cross sections (XY—horizontal direction and Z—building direction) were polished with sandpaper and diamond paste of 1 µm. These polished surfaces were then etched with a 2 vol% Nital solution (HNO_3 and ethanol) for 5 s to visualise the microstructure.

Mechanical testing

Vickers microhardness indentations and tensile tests were performed on the nanocomposites under two different conditions: as-built (before aging treatment) and after aging treatment.

Vickers indentations were performed with a pyramid tip on the polished surface of the specimens according to ASTM E92-17. This pyramid tip was constantly pressed with a force of 2 kgf for 15 s. To ensure consistency of results, six indentations were made using a Duramin model durometer (Struers, Denmark). The mechanical tests included tensile tests and Charpy impact tests. The former were performed three times in succession in a testing machine, model AG -25TA (Shimadzu, Japan), without strain gauge and with a constant displacement rate of the crosshead (0.5 mm/min). The curves obtained were used to graphically determine the yield stress (YS) at 0.2% elongation and the ultimate tensile strength (UTS). Charpy tests were performed to determine the energy required until failure of the nanocomposite materials occurs. A standard vertical pendulum machine (Avery, UK) was used, following the procedures of ASTM E 23–96 with the procedure repeated three times to obtain an average value.

Tribological testing

The wear behaviour of the nanocomposites was investigated by pin-on-disc tests at room temperature (RT). The tribometer used for the tests was a model TE92 (Plint Instruments, UK). The sliding velocity was 0.4 m/s and the pins were pressed with a normal load of 40 N against a polypropylene reinforced with 40 wt% glass fibres (PP40). These conditions, used in our previous studies, are intended to provide measurable and representative wear conditions [40, 42, 43]. The total duration of each test was approximately 30 min (sliding distance approximately 800 m). Prior to each test, both the pin and the disc were carefully cleaned with ethanol, and temperature and humidity conditions were checked to ensure a controlled environment for each test. For each sample, three tests were performed at room temperature. During the tests, the coefficient of friction (COF) was continuously monitored with a load cell. After the tests, the specific wear rate (k) was determined by measuring the actual worn volume by taking three-dimensional profiles of the pins before and after the test using an optical 3D profilometer model S-neox (Sensofar, Spain). Equation (1) was used to calculate k.

$$k = \frac{V}{F \times L} \quad (1)$$

where V (mm^3) is the measured worn volume calculated by superimposing the 3D surface profiles of the pins, F (N) is the

applied force, and L (m) is the total sliding distance after completion of the dry sliding wear test.

The worn surface of the pins was analysed using SEM and EDS.

After the test, the PP40 wear marks were also analysed using SEM/ EDS to evaluate their morphology as well as their chemical composition. In addition, the wear debris (which remained on the surface of the pin after the test) were also analysed with SEM/ EDS.

The results and critical discussion

Feedstock material analysis

Figure 1 (a-c) shows the morphology of the TiC nanopowder in its initial state. Overall, some agglomeration can be seen, and the shape of the nanoparticles is approximately spherical. According to the measurements performed with Image J, the average particle size is 57 nm. The size of the particles ranges from 22 to 141 nm [see size distribution of NPs in Fig. 1(c)].

Figure 1(d–k) shows the morphology of the original steel powder and the starting material for the production of MMNCs after milling with different TiC contents. Overall, the shape of the powder remained approximately spherical. It can also be seen that the surface of the 18Ni300 steel powder is completely covered by TiC when 7.0 vol% was added [Fig. 1(j–k)]. The flowability of the powders was tested by the Hall funnel method following ASTM B213-20 before PBF-LB processing. The three prepared powders flowed freely through the 2.5 mm opening of the hopper under the influence of gravity. The flow time (for 50 grammes) of the starting materials for PBF-LB is summarized in the high magnification images (e, g, i, k). As the concentration of TiC nanoparticles increases, the flow time also increases, indicating a decrease in flowability. The addition of 4.5 vol% and 7.0 vol% resulted in flow times that were relatively higher than those reported for typical powdered materials used in PBF-LB (15 to 30 s) [44]. Nevertheless, the three powders produced were considered for PBF-LB processing.

The XRD diffraction peaks of the starting material powders are shown in Fig. 2(a). The XRD patterns of the reinforcing phase show strong peaks at 41.7°, 60.4°, 76.2°, and 72.3°, corresponding to the TiC phase. The XRD patterns of the 18Ni300 powder show that it is mainly composed of the martensitic phase. This may be due to the high cooling rate during the gas atomization process for powder production [7]. The XRD spectra of the ground powders with the addition of 2.0, 4.5, and 7.0 vol% TiC are similar to those of the maraging steel and also show the presence of martensite, but five new peaks at 2θ of 35.9°, 41.7°, 60.4°, 76.2°, and 72.3° have appeared corresponding

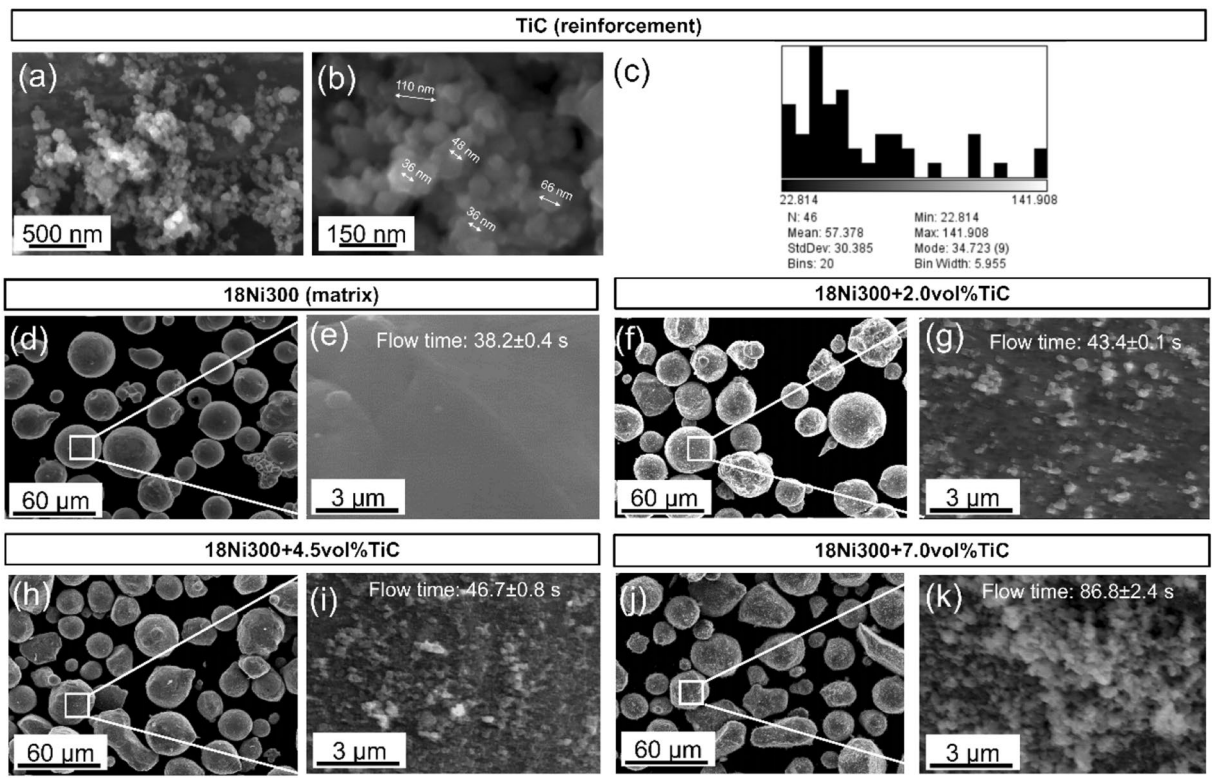

Figure 1: (a-b) SEM of TiC nanopowder at different magnifications; (c) particle size distribution of the nanopowder; (d-k) Morphology of starting feedstock powders after 4-h high-energy ball milling for PBF-LB processing TiC-reinforced 18Ni300 nanocomposites.

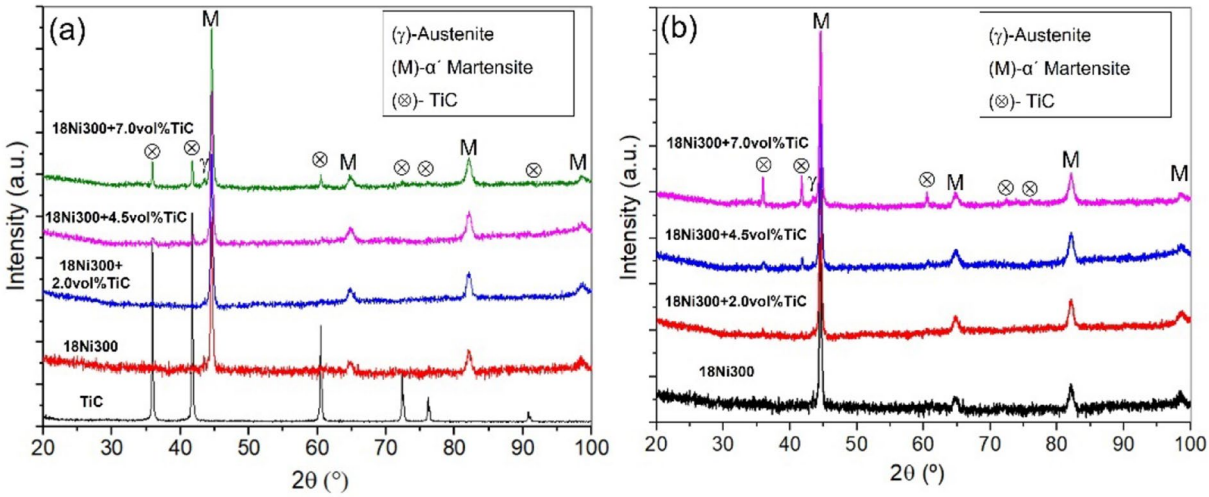

Figure 2: XRD patterns: (a) feedstock powders for PBF-LB; (b) nanocomposite parts after aging treatment.

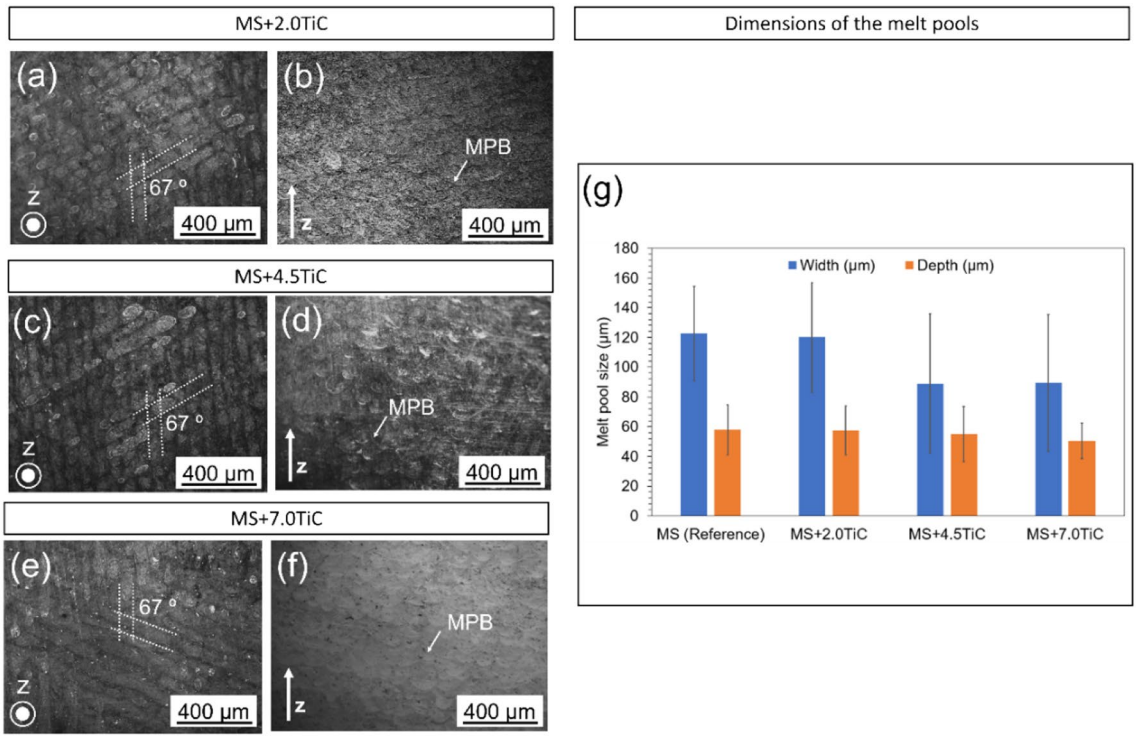

Figure 3: (a–f) Horizontal (XY) and vertical (Z) micrographs of TiC-reinforced 18Ni300 nanocomposites manufactured by PBF-LB after aging treatment; (g) dimensions of the melt pool for the different nanocomposites (measured in the aged and etched condition).

to the TiC. It can also be seen that these peaks have higher intensity at larger concentrations of TiC.

Phases and microstructure of nanocomposites

The XRD patterns recorded for the nanocomposites after aging are shown in Fig. 2(b). In all cases, strong diffraction peaks at 2θ of 44.5°, 64.3°, 81.8°, and 98.5° can be seen, corresponding to the martensite phase (α'-martensite). In addition, the XRD spectra of the 18Ni300 + 2.0 vol% TiC, 18Ni300 + 4.5 vol% TiC and 18Ni300 + 7.0 vol% TiC also show small peaks corresponding to the TiC phase, ensuring the presence of the reinforcement phase.

Figure 3(a–f) shows the microscopic images of the nanocomposites after aging treatment. In the horizontal sections XY [Fig. 3(a), (c) and (e)], the laser tracks can be seen with a

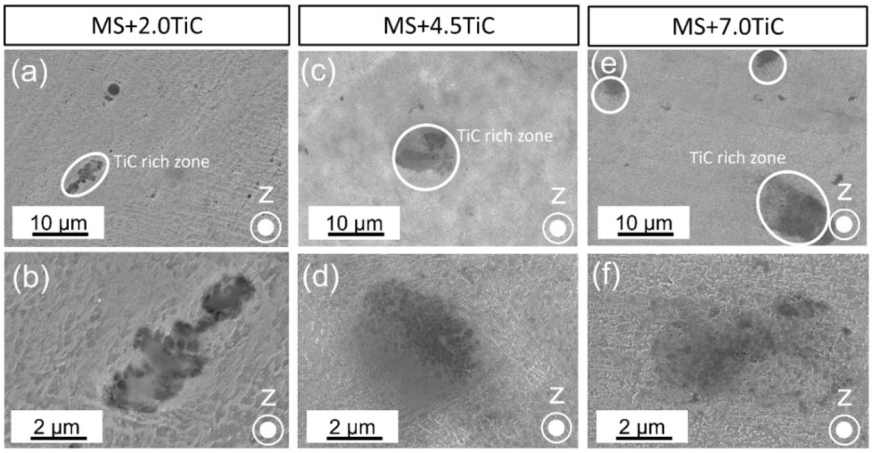

Figure 4: SEM micrographs of the PBF-LB processed 18Ni300/TiC nanocomposites in the aged condition: (a-b) MS + 2.0TiC; (c-d) MS + 4.5TiC; (e–f) MS + 7.0TiC. *(Images (b), (d) and (f) are high magnifications taken in the TiC rich zones).*

rotation angle of 67°, which is due to the scanning strategy used. In the vertical sections Z [Fig. 3(b), (d) and (f)], melt pools, separated by melt pool boundaries (MPB) can be seen. The dimensions of the melt pools were determined using Image J software in the buildup direction (Z) and perpendicular to the buildup direction (XY) and are shown in the graph in Fig. 3(g). It can also be seen that the connections between the laser markings are effective. In all cases, a surface with few pores is observed, which shows that the PBF-LB manufacturing parameters used (laser power 250 W, scanning speed 1000 mm/s, hatch distance 75 µm and layer thickness 50 µm), are in the ideal range for processing these materials.

From Fig. 3(g), it can be seen that the measured width and depth of the melt pool show no statistical difference when different contents of TiC nanoparticles are added. Figure 4 shows the SEM micrographs of the etched cross sections of the nanocomposites manufactured by PBF-LB in the aged state. In MS + 2.0TiC after aging treatment [Fig. 4(a) and (b)], the usual cellular and dendritic microstructure is visible (formed by Ni segregation, but gradually dissolved by heat treatment). In addition, due to their small size, inclusions of TiC with agglomeration are also visible in certain areas. This was confirmed by EDS analysis (not shown) performed on three different locations of these areas. At MS + 2.0TiC, fine cells form in the core of the molten pool and begin to coarsen as they move away from the centerline until they reach the heat-affected zone (HAZ) at the boundary of MPB [27]. The dendrite grains grow in the direction of the increasing temperature gradient (along the centre of the melt pool), which is hindered by the high solidification rate [27, 37, 41, 45]. The addition of a higher amount of TiC (4.5 or 7.0 vol%) resulted in a finer microstructure [Fig. 4(c) to (f)]. This indicates that the addition of TiC NPs can retard grain growth. Similar results can be found in the work of Zhai et al. [46] and AlMangour et al. [27]. Both authors studied 316L stainless steel reinforced with micro- and nano-sized TiC. Zhai et al. [46] reported that the cellular microstructural boundary consists of dislocation associated networks with segregation of alloying elements. They also reported that dissolution of micro-sized TiC into the matrix did not occur due to PBF-LB rapid cooling. AlMangour et al. [27] found that TiC induced nucleation sites due to its good wettability for nucleation of the steel. Liu et al. [47] studied the strengthening mechanism in micro-sized TiC-reinforced AISI 420 stainless steel and reported that the TiC microparticles uniformly connect the grain boundaries and form refined ring-like structures under the influence of local surface tension. In our case, no ring-like structures were observed, probably due to the lack of energy input during the PBF-LB process. AlMangour et al. [48] fabricated 316L/TiC nanocomposites by PBF-LB and found that ring-like structures appeared only at higher energy densities (more than 125 J/mm^3 in their case), but the grain size increased significantly with these energy density values, and the risk of keyhole porosity is higher due to excessive energy density.

Mechanical characterization

TiC-reinforced 18Ni300 nanocomposites were characterized by microhardness, tensile and impact tests and the results are shown in Fig. 5(a) and (b). YS and UTS of the PBF-LB-manufactured 18Ni300 steel (MS (reference)) are also shown in Fig. 5 to compare with the nanocomposites. It can be seen that the YS and UTS values of the 18Ni300 in the as-built state (before aging) are 1063 MPa and 1178 MPa, respectively. After aging treatment, YS and UTS increased to 1942 MPa and 1984 MPa, respectively.

For the nanocomposites, increasing the TiC concentration before aging leads to an increase in both YS and UTS, with the maximum values (1566 MPa for both) reached after the addition of 7.0 vol% of TiC. After the aging treatment [Fig. 5(a)], YS and UTS are higher than the values of the as-built materials and reach their maximum value at a TiC concentration of 4.5 vol% (YS and UTS of 2070 MPa). This fact is due to the typical mechanism of precipitation hardening that occurs in maraging steels

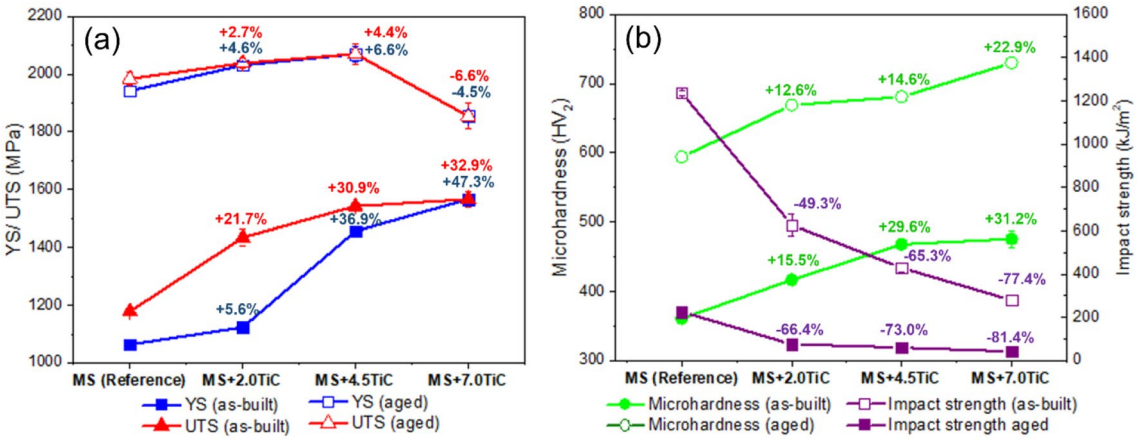

Figure 5: Mechanical properties of the nanocomposites manufactured by PBF-LB: (a) YS and UTS, (b) microhardness and impact strength. (*Note: For comparison, the properties of the unreinforced 18Ni300 material are also shown (labelled "MS (reference)" in the graphs*).

[49]. When nano-TiC is used, it is noteworthy that the material decreases its ability to deform plastically without fracturing, since YS and UTS are quite comparable and even coincide when more than 4.5 vol% TiC is added. The strengthening can be explained by the effect of the Orowan mechanism. According to this mechanism [50], the Orowan strengthening effect ($\Delta\sigma_{Orowan}$) is larger when the particle size of the reinforcement is smaller. In this work, since the average particle size of TiC is in the nanoscale, this effect cannot be ignored [50].

Moreover, large amounts of dislocations accumulate near the TiC particles and the 18Ni300 matrix during solidification, which is due to the mismatch of CTE between the TiC nanoparticles (7.74×10^{-6}/K) and the 18Ni300 matrix (13.0×10^{-6}/K) [50, 51]. Here, the differences in CTE between the TiC reinforcement phase and the 18Ni300 matrix ($\Delta\sigma_{CTE}$) resulted in increased dislocation density [52].

The microhardness values of the PBF-LB-manufactured 18Ni300 steel (MS (reference)) are also plotted in the graph to compare with the nanocomposites. It can be seen that the microhardness of the 18Ni300 in the as-built state (before aging) was 362 HV_2. After aging treatment, the microhardness increased to 595 HV_2.

For the nanocomposites, increasing the TiC concentration tended to increase the microhardness, which reached its maximum value (476 HV_2) for the material reinforced with 7.0 vol% TiC, as in the as-built condition. After aging, a similar conclusion can be drawn, since increasing the TiC concentration led to an increase in microhardness (although less pronounced than before aging due to the dual effect of TiC reinforcement and the hardening mechanism in the maraging steel). The maximum value after aging treatment was observed after the addition of 7.0 vol% TiC (730 HV_2). As for the as-built impact strength [Fig. 5(b)], it can be seen throughout that the increase in TiC concentration contributes to a decrease in the energy required to cause the material to fracture, with the maximum value (1237 kJ/m^2) for the unreinforced material and the minimum value (280 kJ/m^2) observed after the addition of 7.0 vol% TiC. After aging, the material became even more brittle, which can be attributed to the overlapping strengthening effects due to the addition of TiC and the precipitation of intermetallics in the maraging steel. The lowest value (42 kJ/m^2) was observed after the addition of 7.0% TiC. In future studies, the low impact strength could be overcome by heat treatments at lower temperatures or shorter durations to obtain a material with more balanced mechanical properties.

Tribological testing

Pin-on-disc tests were performed to investigate the wear behaviour of the PBF-LB-processed TiC-reinforced 18Ni300 nanocomposites under dry sliding conditions. Figure 6 shows the COF curves recorded during tribological testing of the nanocomposite pins in contact with a PP40 counterpart. In all cases, a running-in period is evident during the first 400 m of sliding distance, until a stable value of about: 0.35 at MS (reference), 0.33 at MS + 2.0TiC, 0.42 at MS + 4.5TiC and 0.43 at MS + 7.0TiC.

Similar trends were reported by Zhao et al. [53] in a study investigating the tribological behaviour of 316L stainless steel reinforced by micro-sized TiC. The authors found that, as the TiC content in the 316L/TiC material increased, the COF values also increased. They attributed this increasing trend to the phenomenon of debris accumulation in the deeper grooves formed in the surface of the material during dry sliding contact. The SEM analysis of the worn surfaces of the pins in Fig. 7 shows that the grooves in the pins are more pronounced in the material reinforced with a high TiC content (above 4.5 vol%) and are caused by material deformation rather than severe abrasion, which occurs in the material reinforced with less than 4.5 vol%.

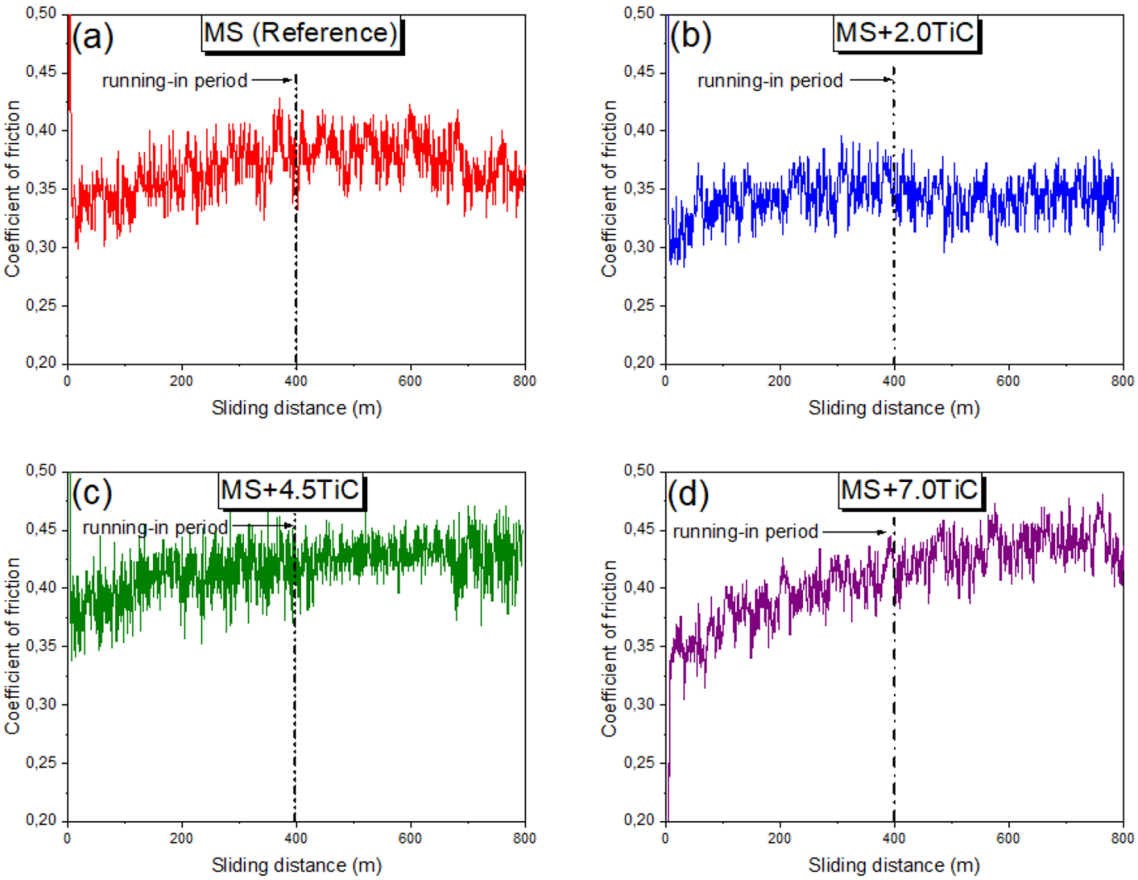

Figure 6: Representative COF curves recorded during tribological tests under dry sliding between nanocomposite pins and PP40.

Wear debris can accumulate in these grooves, contributing to an increase in COF values.

As Fig. 7 shows, as the TiC reinforcement content increased, less material was removed from the pins, as seen in the 3D profiles, which is reflected in a smaller k. As mentioned in our previous study [40], MS exhibits abrasive scratches after sliding against glass fibre reinforced polypropylene, suggesting abrasive wear. In the case of the material reinforced with 2.0 vol% TiC, abrasion due to cyclic loading and hard irregularities of the glass seems to be the cause of the material loss. The large width of the wear grooves visible in the material reinforced with more than 4.5 vol% TiC may indicate abrasion, but it may also indicate fatigue wear, which causes severe deformation but little material removal. As discussed in [54], material removal by fatigue is more difficult than by abrasion because multiple deformations and displacements are required to remove material.

By superimposing the two 3D profiles of the pins (before and after testing), the volume of lost material was determined for each case. Figure 8 shows the average volume of worn material and the calculated k. The worn volume is higher for the unreinforced material, MS (6.59×10^{-2} mm^3) than for MS + 2.0TiC, MS + 4.5TiC, and MS + 7.0TiC (2.41×10^{-2}, 2.12×10^{-2}, and 1.04×10^{-2} mm^3, respectively). As for the specific wear rate, a decrease of 59.2% for MS + 2.0TiC, 63.0% for MS + 4.5TiC, and 82.6% for MS + 7.0TiC is observed compared to the unreinforced steel, indicating better wear performance due to the nanoscale TiC reinforcement phase. These results show a good correlation with the evolution of microhardness in the aged condition. It can be seen that the nanocomposites with the higher microhardness have a lower specific wear rate, as classically predicted by Archard's law [55].

Figure 9 shows the k of the PP40 material after sliding on the different nanocomposites and the corresponding three-dimensional profiles obtained by 3D profilometry.

The track resulting from the sliding of MS + 2.0TiC is the deepest (40 μm on average). In other cases, the tracks are less deep but wider, and the width is largest when the dry sliding tests were performed against MS + 7.0TiC. This could be due to thermal phenomena caused by the friction generated. As discussed in our previous work [40], greater friction leads to greater fictional heat, which in turn softens the polymer so that the material removal is smoother and the track tends to be wider (this is particularly observed in the cases where MS + 4.5TiC and MS + 7.0TiC pins were used). In the case where less fictional heat

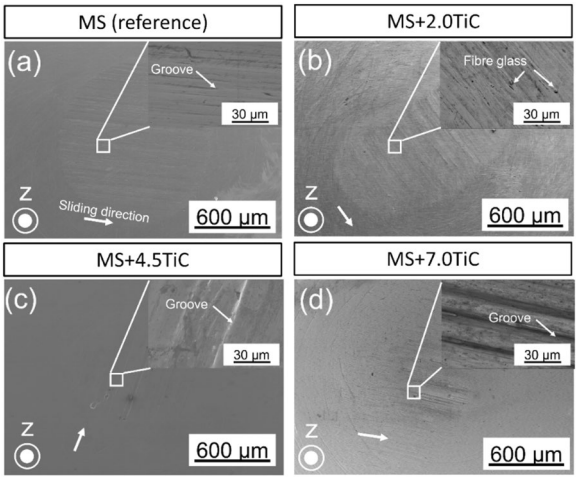

Figure 7: SEM of the pin´s worn surfaces: (a) MS (reference), (b) MS + 2.0TiC, (c) MS + 4.5TiC, and (d) MS + 7.0TiC. (The sliding direction is indicated by the white arrows; the PBF-LB building direction is also given).

was generated on the surface of the PP40, the track is deeper than MS and has a similar width as when using MS (1270 µm), which can be attributed to the more brittle state of the PP40.

As seen in Fig. 8, the material reinforced with 7.0vol% TiC showed the lowest specific wear rate after sliding against the PP40 disc. In addition, the higher COF value (0.43) caused a larger wear volume on the PP40 disc. In practise, this suggests that using MS + 7.0TiC material in a mould would result in longer life, but also that higher injection pressures must be used to overcome the higher friction between the viscous polymer-reinforced material and the mould wall. Since the material is injected in a viscous state and then solidifies in contact with the mould wall, the risk of defects in the parts during injection contact is avoided.

The analysis of the wear mechanisms in dry sliding is important because when the parts are demoulded, there is contact between the mould surface and the solid part, which can cause damage to the injected parts.

The SEM analysis of the PP40 wear track, suggests that the mechanisms contributing to PP40 wear depend on the composition of the contact material (pin). In our previous work [40], it was discussed that the analysis of the wear track morphology, i.e., the presence of plastic deformation or the presence of microcracks, is related to the frictional heat generated during the sliding contact. If if the fictional heat is high enough to soften the polypropylene, this will cause local melting in the track, while lower fictional heat will cause a more brittle polymer, which will promote the appearance of microcracks in the wear track. Based on the COF values recorded for the different tribological pairs (Fig. 6), the same trend can be confirmed. A smaller COF value (~ 0.33) in the MS + 2.0TiC-PP40 [Fig. 10(b)] resulted in a track with microcracks. On the other hand, the track in PP40 derived from the tribological pairs with higher COF values (MS + 4.5TiC and MS + 7.0TiC, with COF values of ~ 0.42 and 0.43, respectively), as shown in Fig. 10(c) and (d), showed no signs of microcracking, but some plastic deformation that could have been caused by the softening of the polymer. In the analysis of EDS (not shown), the presence of Fe in the track was observed only at MS and MS + 2.0TiC. The

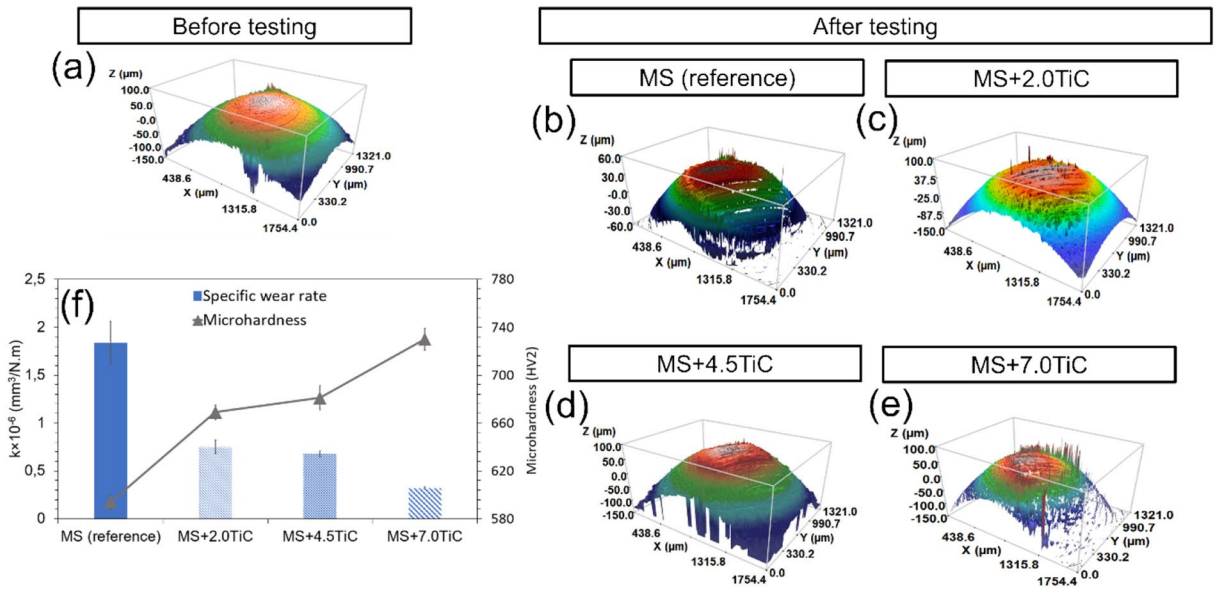

Figure 8: Representative 3D profiles of the pins (a) before and (b)-(e) after the tribological testing; (f) specific wear rate of different nanocomposites and microhardness after testing.

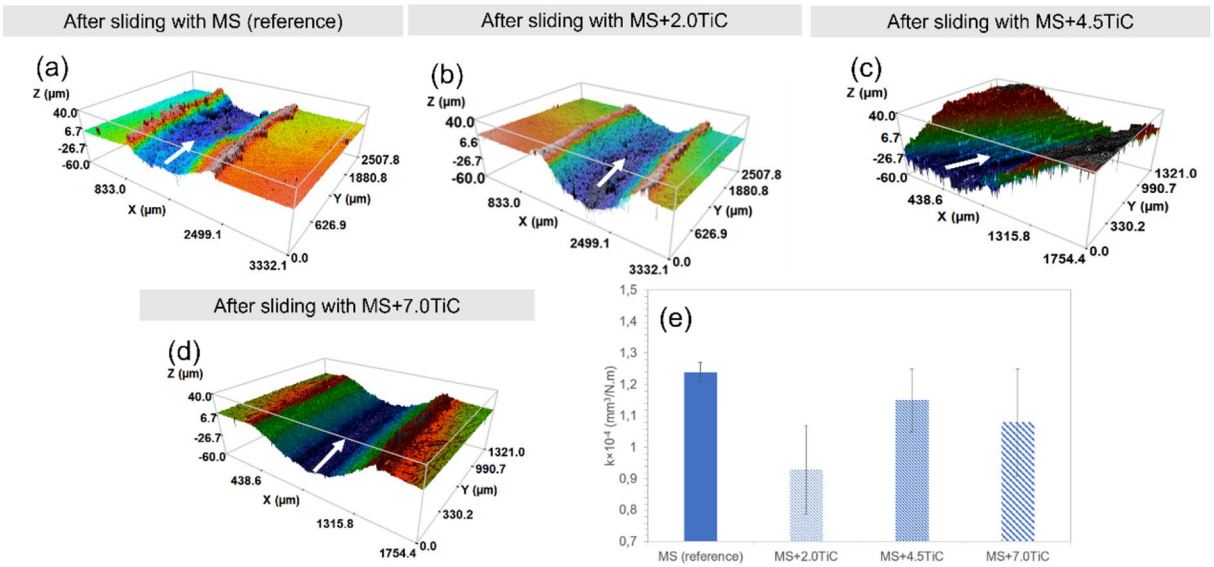

Figure 9: (a–d) Representative 3D profiles of the PP40 wear tracks after the testing; (e) specific wear rate of the PP40 material after the dry sliding wear tests with the different nanocomposite materials.

presence of TiC was not detected in any of the cases, probably due to its low volume.

The different wear mechanisms that occur on the track lead to differences in the morphology of the wear debris. SEM analysis of the wear debris is shown in Fig. 10(e–h). As described in our study [40], the wear debris generated during sliding of MS against PP40 consist mainly of roll-shaped debris [Fig. 10(e)] with a proportion of larger and irregular particles. This is due to the frictional heat released during sliding contact, which contributes to the softening of the polymer, so that the wear debris particles take on a roll-like shape due to the softened polymer roll between the pin and the disc. EDS analysis showed the presence of Fe. Similarly, it can be observed that the wear debris formed when the pin of MS + 2.0TiC slides against the PP40 [Fig. 10(f)] consist of both irregular and roll-like fragments, with Fe present (as a wear track). The wear debris consist of glass fibres and Fe soaked in polypropylene, which were extracted due to the more brittle state of the polymer, as the lower COF [Fig. 6(b)] generates less frictional heat. When testing the pins MS + 4.5TiC and MS + 7.0TiC against PP40, only roll-like debris were observed (Fig. 10(g) and (h), respectively). In these cases, elemental Fe was not observed in the debris in the analysis of EDS (not shown), indicating that no material was transferred of material from the pin to the PP40 (or only very small amounts). Unlike the previous cases (MS and MS + 2.0TiC), the tracks on the PP40 are wider, probably due to the higher fictional heat (due to the higher COF), which favours polymer softening and plastic deformation.

Conclusions

TiC-reinforced 18Ni300 formulations were developed, and the nanocomposites were successfully fabricated by PBF-LB. The main conclusions can be summarised as follows:

- TiC-reinforced 18Ni300 steel exhibits significantly higher YS and UTS than unreinforced 18Ni300 steel, due to its refined microstructure and TiC-induced strengthening effect.
- TiC-reinforced 18Ni300 nanocomposites showed better wear resistance than the unreinforced 18Ni300 steel, and the lowest specific wear rate was found for the 18Ni300 steel reinforced with 7.0 vol% TiC: $k = 0.32 \times 10^{-6}$ mm^3/N.m versus $k = 1.84 \times 10^{-6}$ mm^3/N.m for the unreinforced 18Ni300 steel.
- Abrasion was found to be the main wear mechanism for both the unreinforced 18Ni300 and the 18Ni300 reinforced with 2.0 vol% TiC, while for the steel reinforced with 4.5 and 7.0 vol%, TiC material removal due to abrasion and signs of material fatigue could be the cause of wear.
- The addition of large amounts of TiC reduced the impact strength of the material and made it extremely brittle, especially after aging treatment.
- The aging treatment should be optimised to better balance the elastic properties of the nanocomposites (e.g., shorter aging or lower temperatures).
- Overall, the results show that the PBF-LB-produced TiC-reinforced 18Ni300 nanocomposites are promising for use in mould components, especially in inserts subject to severe wear, such as PP40 injection.

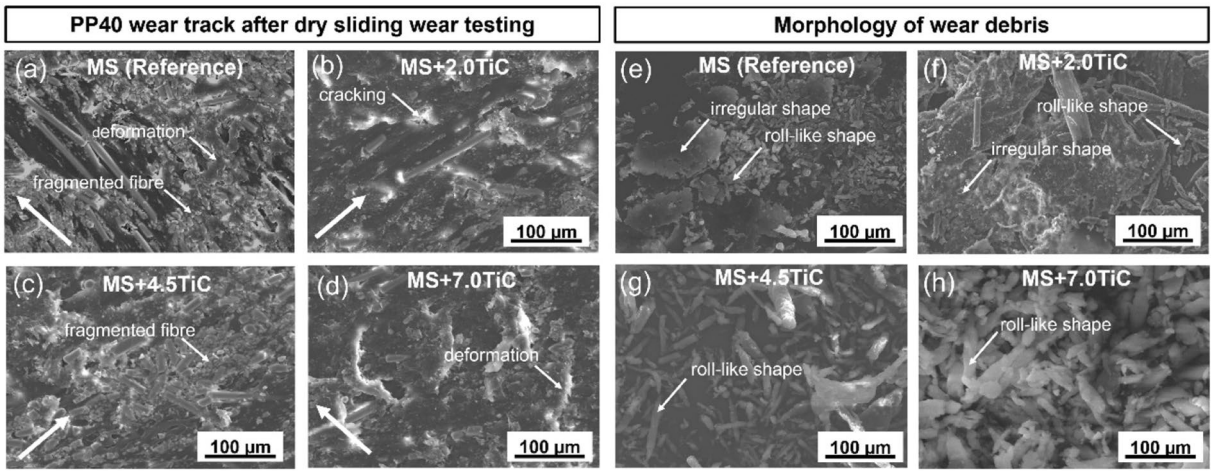

Figure 10: (a–d) SEM of the PP40 wear tracks after the dry sliding wear tests with the different nanocomposite materials (The sliding direction is indicated by the white arrows); (e–h) Representative SEM morphology of wear debris originated during the tribological test of PP40 against: (a) MS (reference), (b) MS + 2.0TiC; (c) MS + 4.5TiC and (d) MS + 7.0TiC.

Acknowledgments

Special acknowledgements are due to the partner of this study: Simoldes Aços company (Oliveira de Azeméis, Portugal) for the support and assistance with PBF-LB steel sample's manufacturing.

Funding

Open access funding provided by FCT|FCCN (b-on). This work was developed within the scope of the project CICECO-Aveiro Institute of Materials, UIDB/50011/2020 & UIDP/50011/2020, financed by national funds through the Portuguese Foundation for Science and Technology/MCTES and supported by the European Regional Development Fund—ERDF, through POCI-01–0247-FEDER-039842.

Data availability

Data will be made available on reasonable request.

Declarations

Conflict of interest The authors declare that they have no known competing financial interests or personal relationships that could have appeared to influence the work reported in this paper.

Open Access

References

1. V.G. Smelov, A.V. Sotov, A.V. Agapovichev, M.M. Laktionova, T.M. Tomilina, Implementation of the additive technology to the design and manufacturing of vibroisolators with required filtering. Proc. Eng. **176**, 540–545 (2017)
2. T. Trosch, J. Strößner, R. Völkl, U. Glatzel, Microstructure and mechanical properties of selective laser melted Inconel 718 compared to forging and casting. Mater. Lett. **164**, 428–431 (2016)
3. P. Ponnusamy, R.A. Rahman Rashid, S.H. Masood, D. Ruan, S. Palanisamy, Mechanical properties of SLM-printed aluminium alloys: A review. Materials **13**(19), 4301 (2020)
4. N.J. Harrison, I. Todd, K. Mumtaz, Reduction of micro-cracking in nickel superalloys processed by Selective Laser Melting: A fundamental alloy design approach. Acta Mater. **94**, 59–68 (2015)
5. L. Wu et al., Hot work tool steel processed by laser powder bed fusion: A review on most relevant influencing factors. Adv. Eng. Mater. **23**(7), 2100049 (2021)
6. J. Sander, J. Hufenbach, L. Giebeler, H. Wendrock, U. Kühn, J. Eckert, Microstructure and properties of FeCrMoVC tool steel produced by selective laser melting. Mater. Des. **89**, 335–341 (2016). https://doi.org/10.1016/j.matdes.2015.09.148

7. J. Yan, Y. Zhou, R. Gu, X. Zhang, W.-M. Quach, M. Yan, A comprehensive study of steel powders (316L, H13, P20 and 18Ni300) for their selective laser melting additive manufacturing. Metals (Basel) **9**(1), 86 (2019)
8. I. Tolosa, F. Garciandía, F. Zubiri, F. Zapirain, A. Esnaola, Study of mechanical properties of AISI 316 stainless steel processed by 'selective laser melting', following different manufacturing strategies. Int. J. Adv. Manuf. Technol. **51**(5), 639–647 (2010)
9. O. Fashanu et al., Effect of SLM build parameters on the compressive properties of 304L stainless steel. J. Manuf. Mater. Process. **3**(2), 43 (2019)
10. X. Zhao et al., Fabrication and characterization of AISI 420 stainless steel using selective laser melting. Mater. Manuf. Processes **30**(11), 1283–1289 (2015)
11. X.P. Li et al., Selective laser melting of nano-TiB2 decorated AlSi10Mg alloy with high fracture strength and ductility. Acta Mater. **129**, 183–193 (2017)
12. D.Q. Zhang, Z.H. Liu, Q.Z. Cai, J.H. Liu, C.K. Chua, Influence of Ni content on microstructure of W-Ni alloy produced by selective laser melting. Int. J. Refract. Metals Hard Mater. **45**, 15–22 (2014)
13. C.Y. Yap, H.K. Tan, Z. Du, C.K. Chua, Z. Dong, Selective laser melting of nickel powder. Rapid Prototyp. J. **23**(4), 750–757 (2017)
14. Z.X. Khoo, Y. Liu, J. An, C.K. Chua, Y.F. Shen, C.N. Kuo, A review of selective laser melted NiTi shape memory alloy. Materials **11**(4), 519 (2018)
15. J. Li et al., Tribological behavior of TiC particles reinforced 316Lss composite fabricated using selective laser melting. Materials **12**(6), 950 (2019)
16. R. Branco et al., Low-cycle fatigue behaviour of AISI 18Ni300 maraging steel produced by selective laser melting. Metals (Basel) **8**(1), 32 (2018)
17. C. Tan et al., Design and additive manufacturing of novel conformal cooling molds. Mater. Des. **196**, 109147 (2020)
18. A.C. Long, C.E. Wilks, C.D. Rudd, Experimental characterisation of the consolidation of a commingled glass/polypropylene composite. Compos. Sci. Technol. **61**(11), 1591–1603 (2001)
19. A.S. Pouzada, E.C. Ferreira, A.J. Pontes, Friction properties of moulding thermoplastics. Polym. Test **25**(8), 1017–1023 (2006)
20. W.H. Yu, S.L. Sing, C.K. Chua, C.-N. Kuo, X.L. Tian, Particle-reinforced metal matrix nanocomposites fabricated by selective laser melting: A state of the art review. Prog. Mater. Sci. **104**, 330–379 (2019)
21. Y. Hu, W. Cong, A review on laser deposition-additive manufacturing of ceramics and ceramic reinforced metal matrix composites. Ceram. Int. **44**(17), 20599–20612 (2018)
22. N. Li et al., Progress in additive manufacturing on new materials: A review. J. Mater. Sci. Technol. **35**(2), 242–269 (2019)
23. B. AlMangour, D. Grzesiak, J.-M. Yang, Rapid fabrication of bulk-form TiB2/316L stainless steel nanocomposites with novel reinforcement architecture and improved performance by selective laser melting. J. Alloys Compd. **680**, 480–493 (2016)
24. S. Dadbakhsh, R. Mertens, L. Hao, J. Van Humbeeck, J. Kruth, Selective laser melting to manufacture 'in situ' metal matrix composites: a review. Adv. Eng. Mater. **21**(3), 1801244 (2019)
25. H. Chen et al., Achieving high strength and high ductility in WC-reinforced iron-based composites by laser additive manufacturing. Addit. Manuf. **35**, 101195 (2020)
26. N. Kang, W. Ma, F. Li, H. Liao, M. Liu, C. Coddet, Microstructure and wear properties of selective laser melted WC reinforced 18Ni-300 steel matrix composite. Vacuum **154**, 69–74 (2018)
27. B. AlMangour, D. Grzesiak, Selective laser melting of TiC reinforced 316L stainless steel matrix nanocomposites: Influence of starting TiC particle size and volume content. Mater. Des. **104**, 141–151 (2016)
28. H. Dieringa, Production and properties of light metal matrix nanocomposites. Metals **10**, 95 (2020)
29. D. Gu, P. Yuan, Thermal evolution behavior and fluid dynamics during laser additive manufacturing of Al-based nanocomposites: Underlying role of reinforcement weight fraction. J. Appl. Phys. **118**(23), 233109 (2015)
30. B. Zheng, J.E. Smugeresky, Y. Zhou, D. Baker, E.J. Lavernia, Microstructure and properties of laser-deposited Ti6Al4V metal matrix composites using Ni-coated powder. Metall. Mater. Trans. A. **39**(5), 1196–1205 (2008)
31. A. Bhowmik, W. Zhai, W. Zhou, S.M.L. Nai, Characterization of carbide particle-reinforced 316L stainless steel fabricated by selective laser melting. Mater. Charact. **179**, 111360 (2021)
32. A.P. Oliveira, L.H.Q.R. Lima, B.C.A. Felipe, C. Bolfarini, R.T. Coelho, P. Gargarella, Effect of microstructure and defect formation on the bending properties of additive manufactured H13 tool steel. J. Market. Res. **15**, 3598–3609 (2021)
33. M. Kahlert, F. Brenne, M. Vollmer, T. Niendorf, Influence of microstructure and defects on mechanical properties of AISI H13 manufactured by electron beam powder bed fusion. J. Mater. Eng. Perform. **30**, 6895–6904 (2021)
34. B. AlMangour, D. Grzesiak, J.-M. Yang, Nanocrystalline TiC-reinforced H13 steel matrix nanocomposites fabricated by selective laser melting. Mater. Des. **96**, 150–161 (2016)
35. L. Hao, S. Dadbakhsh, O. Seaman, M. Felstead, Selective laser melting of a stainless steel and hydroxyapatite composite for load-bearing implant development. J. Mater. Process. Technol. **209**(17), 5793–5801 (2009)
36. J. Hu, H. Zhu, J. Zhang, M. Ouyang, C. Qiu, J. Duan, Effects of TiC addition on microstructure, microhardness and wear resistance of 18Ni300 maraging steel by direct laser deposition. J. Mater. Process. Technol. **296**, 117213 (2021)
37. A.J. Pinkerton, L. Li, The effect of laser pulse width on multiple-layer 316L steel clad microstructure and surface finish. Appl. Surf. Sci. **208**, 411–416 (2003)

38. Renishaw, Design for metal AM - a beginner's guide. Renishaw Newslett. **44**, 1–16, 2017, [Online]. Available: https://www.renishaw.com/en/design-for-metal-am-a-beginners-guide--42652
39. D.F.S. Ferreira, G. Miranda, F.J. Oliveira, J.M. Oliveira, Predictive models for an optimized fabrication of 18Ni300 maraging steel for moulding and tooling by Selective Laser Melting. J Manuf Process **70**(July), 46–54 (2021)
40. D.F.S. Ferreira, J.S. Vieira, S.P. Rodrigues, G. Miranda, F.J. Oliveira, J.M. Oliveira, Dry sliding wear and mechanical behaviour of selective laser melting processed 18Ni300 and H13 steels for moulds. Wear **488–489**(July), 2022 (2021)
41. S. Yin et al., The influence of aging temperature and aging time on the mechanical and tribological properties of selective laser melted maraging 18Ni-300 steel. Addit Manuf **22**(June), 592–600 (2018). https://doi.org/10.1016/j.addma.2018.06.005
42. H. Unal, A. Mimaroglu, Friction and wear behaviour of unfilled engineering thermoplastics. Mater. Des. **24**(3), 183–187 (2003)
43. H. Unal, U. Sen, A. Mimaroglu, Dry sliding wear characteristics of some industrial polymers against steel counterface. Tribol. Int. **37**(9), 727–732 (2004)
44. J.A. Muñiz-Lerma, A. Nommeots-Nomm, K.E. Waters, M. Brochu, A comprehensive approach to powder feedstock characterization for powder bed fusion additive manufacturing: a case study on AlSi7Mg. Materials **11**(12), 2386 (2018)
45. B. Vrancken, L. Thijs, J.-P. Kruth, J. Van Humbeeck, Heat treatment of Ti6Al4V produced by Selective Laser Melting: Microstructure and mechanical properties. J. Alloys Compd. **541**, 177–185 (2012)
46. W. Zhai, Z. Zhu, W. Zhou, S.M.L. Nai, J. Wei, Selective laser melting of dispersed TiC particles strengthened 316L stainless steel. Compos. B Eng. **199**, 108291 (2020)
47. Y. Liu, M. Tang, Q. Hu, Y. Zhang, L. Zhang, Densification behavior, microstructural evolution, and mechanical properties of TiC/AISI420 stainless steel composites fabricated by selective laser melting. Mater. Des. **187**, 108381 (2020)
48. B. AlMangour, D. Grzesiak, J. Cheng, Y. Ertas, Thermal behavior of the molten pool, microstructural evolution, and tribological performance during selective laser melting of TiC/316L stainless steel nanocomposites: Experimental and simulation methods. J. Mater. Process. Technol. **257**, 288–301 (2018)
49. H.M. Zhu, J.W. Zhang, J.P. Hu, M.N. Ouyang, C.J. Qiu, Effects of aging time on the microstructure and mechanical properties of laser-cladded 18Ni300 maraging steel. J. Mater. Sci. **56**(14), 8835–8847 (2021)
50. L. Chen, Y. Sun, L. Li, X. Ren, Microstructure evolution, mechanical properties, and strengthening mechanism of TiC reinforced Inconel 625 nanocomposites fabricated by selective laser melting. Mater. Sci. Eng. A **792**, 139655 (2020)
51. S. Braccini et al., The maraging-steel blades of the Virgo super attenuator. Meas. Sci. Technol. **11**(5), 467 (2000)
52. N. Srivastava, G.P. Chaudhari, Microstructural evolution and mechanical behavior of ultrasonically synthesized Al6061-nano alumina composites. Mater. Sci. Eng. A **724**, 199–207 (2018)
53. Z. Zhao et al., Microstructure and mechanical properties of TiC-reinforced 316L stainless steel composites fabricated using selective laser melting. Metals (Basel) **9**(2), 267 (2019)
54. S. Gialanella, A. Malandruccolo, *Aerospace alloys* (Springer, Berlin, 2020)
55. M. Hanief, M.S. Charoo, Archard's wear law revisited to measure accurate wear coefficient considering actual sliding velocity. Mater. Today Proc. **47**, 5598–5600 (2021)